

Date of publication xxxx 00, 0000, date of current version xxxx 00, 0000.

Digital Object Identifier 10.1109/ACCESS.2022.Doi Number

Novel Multi-Stage Feedback Technique for Time Skew Calibration in Time-Interleaved ADCs

MIN HU¹, PENGXING YI¹, Senior Member, IEEE, ZHENGXU HAO¹, ZHITONG ZHOU¹

¹Mechanical Science & Engineering, Huazhong University of Science & Technology, Wuhan, 430074, China

Corresponding author: Pengxing Yi (e-mail: pxyi@hust.edu.cn).

This work was supported in part by the China Key Research and Development Plan Project [2018YFB2003303].

ABSTRACT This paper introduces a novel low-complexity algorithm for time skew calibration, which is crucial in ensuring undistorted signal acquisition in a time-interleaved analog-to-digital conversion system. By approximating the absolute value of the difference during linear approximation, the algorithm decouples derivatives from the step size factor, significantly reducing computational complexity. An enhanced multi-stage feedback approach is employed to minimize Taylor series approximation errors without increasing the number of derivative calculations. Simulation results demonstrate notable improvements, with an SNDR above 66 dB and an SFDR above 69 dB achieved for single-tone sinusoidal signals after calibration. The algorithm remains effective for multi-tone and frequency modulation signals, demonstrating its versatility. Real-world experimental measurements validate the algorithm's efficacy, highlighting its potential for practical applications with reasonable resource utilization. The proposed multi-stage feedback calibration technique consumes 1509 look-up tables (LUTs), 1409 flip flops (FFs), 33 Inputs/Outputs (I/Os), 1 buffer-global-clock (BUFG), 33 digital signal processors (DSPs), and 16.5 block random access memories (BRAMs) in the implementation, making it a practical solution for various applications.

INDEX TERMS Time-interleaved, digital calibration, time skew, multi-stage feedback approach, fewer derivatives

I. INTRODUCTION

Digital communication receivers play a pivotal role in modern communication technologies. However, with the relentless advancement of technologies such as 4G/5G wireless base stations, broadband satellite receivers, and software-defined radios, these receivers are now subject to increasing demands for higher sampling rates and broader bandwidths. To address this pressing challenge, Time-Interleaved Analog-to-Digital Conversion Systems (TI-ADCs) have emerged as a groundbreaking solution. As proposed in reference [1], TI-ADCs involve M pipelined ADCs, each operating at a different sampling clock. Consequently, compared to a single-channel ADC, TI-ADCs have increased by a factor of M . Currently, TI-ADCs are typically constructed using pipelined ADCs to meet ultra-high-speed sampling requirements.

The pipelined ADC is made using Complementary Metal Oxide Semiconductor (CMOS) technology. Additionally, integrated circuits produced by CMOS technology below 90nm have considerable performance differences because of changes in the process [2]. Therefore, it is inevitable that

there will be performance differences between the different sub-ADCs. The performance differences between the sub-ADCs will affect the correct reorganization of the data collected by the sub-ADC. If there are mismatches in the TI-ADCs system, they will degrade the spurious-free dynamic range (SFDR), signal-to-noise ratio (SNR), signal-to-noise distortion ratio (SNDR) and effective number of bits (ENOB). Therefore, analog or digital methods need to be employed to calibrate these mismatches. These mismatches usually include offset, gain, time skew and bandwidth mismatch [26]. Among them, time skew has a significant impact on TI-ADCs and is a nonlinear error. Therefore, there are lots of researchers [3-22] studying how to calibrate time skew. Next, we propose a new algorithm to calibrate time skew.

Currently, the research on calibration technology of time skew in the TI-ADCs mainly focuses on the following aspects: 1) the algorithm's resource usage [3-5], [28-29]; 2)

TABLE I
ADVANTAGES AND LIMITATIONS OF ALGORITHMS

Time skew calibration method	Advantage	Limitation
Polyphase decomposition [20]	Input at any Nyquist	Extensive iterative and derivative computations, high derivative complexity
Expectation of the absolute difference [21]	The input signals of adjacent channels are calculated by difference rather than multiplication	Poor portability
Variable step-size iterative [22]	Fast convergence, low derivative complexity	Additional division module
Correlation-based [23]	No costly matrix multiplication processing, multi-stage calibration	Relevance of estimation process for each channel, complexity of high-order derivatives
Modulation Matrix [24]	No costly matrix multiplication processing, independent estimation process of each channel	Extensive iterative and derivative computations, high derivative complexity
Reference Assisted [31]	Signal-independent	Additional hardware consumption, Large number of derivative calculations during iteration

the calibration of the sub-sampling TI-ADCs [6-9], [30]; 3) the expansion of the frequency band range of the input signal [10-12]; 4) the expansion of the range of time skew [13-16], [27]; 5) reducing the impact of noise on the calibration algorithm [17-18]. Among them, many researchers focus on aspects 1) and 3), such as [20-24].

TABLE I shows the advantages and limitations of time skew calibration algorithms [20-24], [31]. The algorithms in references [21] and [31] rely on supplementary hardware modules, thus limiting their portability and adaptability. Therefore, we present a fully digital calibration approach specifically designed to address time skew. This approach is engineered to improve the portability of the algorithm, ensuring seamless integration and adaptability across various platforms and systems.

In addition, the methods described in references [20-24] and [31] all require calibrated output signals for iteration during the process. Digital correction methods for output signals often entail the use of numerous multiplication and addition units. Therefore, reducing the number of iterations can significantly decrease computational resources, as mentioned in reference [22]. However, the approach in [22] to reduce iterations involves the introduction of division operations. We take a different approach by approximating the absolute value of the arithmetic difference during the linear approximation process. This method eliminates the need to calibrate the output signal during each iteration. For calibration algorithms that employ first-order statistics, such as those

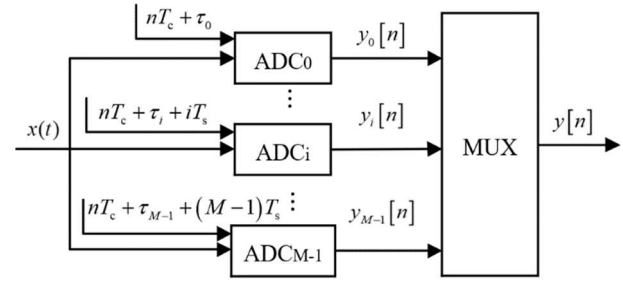


FIGURE 1. Schematic implementation of an M-channel TI-ADC with timing skew.

described in references [22], [23], and [31], this approach successfully saves considerable computational resources in each iteration.

Recognizing the challenges associated with the influence of Taylor series approximation errors in [23] and [31], we introduce an improved multi-stage feedback mechanism. This innovative mechanism effectively mitigates the influence of Taylor series approximation errors on calibration outcomes, while not significantly increasing the computational burden associated with derivative calculations compared to references [23] and [31]. This advancement not only enhances the accuracy of our calibration process but also contributes to its efficiency and practicality.

In summary, the proposed method has two highlights compared to existing calibration algorithms:

- During the iteration process of the algorithm, there is no need to correct the time skew of the output signal. Therefore, the proposed algorithm has a lower computational complexity.
- The improved multi-stage feedback technique achieves a more accurate estimation of time skew than the first-order Taylor series estimation by performing a single derivative of the output signal.

The remainder of this article is organized as follows. Section II introduces the influence of time skew on the TI-ADCs and the technique for correcting time skew. Section III details the efficient implementation of a time skew calibration algorithm characterized by low derivative complexity. Section IV verifies the effectiveness of the proposed techniques, and compares the proposed technique with advanced techniques by simulation results. Section V proves the effectiveness of the proposed techniques by experimental results, and shows the consumption of resources by the proposed techniques. Section VI draws a conclusion.

II. THE TI-ADCs MODEL AND TIME SKEW CORRECTION TECHNIQUES

A. THE INFLUENCE OF TIME SKEW ON THE TI-ADCs

Fig. 1 shows the schematic implementation of an M-channel TI-ADC with timing skew. The input signal $x(t)$ is

alternately sampled by all sub-ADCs with a sampling interval of T_s . The sampling interval of sub-ADCs is T_c . If all mismatches in the TI-ADC except for time skew have been corrected, and the time skew of the i -th sub-ADC is τ_i . Then, the output of each sub-ADC is merged into the output $y[n]$ of the TI-ADC after passing through the multiplexer (MUX).

The output of the i -th channel can be represented as

$$\begin{aligned} y_i[n] &= y[Mn+i] \\ &= x(nT_c + iT_s + \tau_i). \end{aligned} \quad (1)$$

The Discrete-Time Fourier Transform (DTFT) of $y[n]$ can be expressed as [4]

$$\begin{aligned} Y(e^{j\omega}) &= \frac{1}{M} \sum_{i=0}^{M-1} \sum_{k=0}^{M-1} \left(X \left(e^{j\left(\omega - \frac{2\pi k}{M}\right)} \right) \right. \\ &\quad \left. H_i \left(e^{j\left(\omega - \frac{2\pi k}{M}\right)} \right) e^{j\frac{2\pi ki}{M}} \right) \end{aligned} \quad (2)$$

In a TI-ADC system where only time skew is considered, the transfer function of the sub-ADC can be represented as

$$H_i(e^{j\omega}) = e^{j\omega\tau_i} \quad (3)$$

From equation (2) and (3), it becomes evident that time skew results in a difference between the output signal $Y(e^{j\omega})$ and the input signal $X(e^{j\omega})$. Specifically, the distortion in the output signal $X(e^{j\omega})$ arises from the existence of time skew. The purpose of this paper is to mitigate the distortion effect by reducing time skew in this system.

B. TIME SKEW CORRECTION TECHNIQUE

Assuming that in an ideal case, the output signal in a channel time-interleaved sampling system is $x[n]$, then the output after sampling by the i -th sub-ADC can be expressed as:

$$x_i[n] = x[nM+i], i = 0, 1, \dots, M-1. \quad (4)$$

When only considering the time skew τ_i among the M channels, the output of the i -th channel can be expressed as:

$$y_i[n] = x_i \left[n + \frac{\tau_i}{T_c} \right]. \quad (5)$$

The Taylor series is used to calibrate time skew [25]:

$$x_i[n] = y_i[n] + \tau_i \times \nabla y_i[n]. \quad (6)$$

According to equation (6), the time skew can be corrected by using the derivative of the output signal.

III. PROPOSED TIME SKEW CALIBRATION TECHNIQUES

A. AN ITERATIVE ALGORITHM FOR ALGORITHM FOR CALIBRATING TIME SKEW WITHOUT

REQUIRING THE CALIBRATED OUTPUT DURING ITERATIONS

If the input signal can be linearly approximated [22], the difference between the time skew of the $(i+1)$ -th channel and the i -th channel can be expressed as

$$\tau_{i+1} - \tau_i \approx \frac{\sum_{n=1}^L |\Delta y_i[n]| - \Delta}{\nabla}. \quad (7)$$

Where L is the number of samples required to satisfy statistical characteristics. Additionally, there are

$$\Delta y_i[n] = y_{i+1}[n] - y_i[n], \quad (8)$$

$$\Delta = \frac{\sum_{i=0}^{M-2} \sum_{n=1}^L |\Delta y_i[n]| + \sum_{n=1}^L |y_0[n+1] - y_{M-1}[n]|}{M}, \quad (9)$$

$$\nabla = \frac{\sum_{i=0}^{M-1} \sum_{n=1}^L |y'_i[n]|}{M}. \quad (10)$$

There is no need to calculate the product between the outputs of adjacent channels in estimating time skew with equation (7). However, there are matrix calculations in reference [22]. In reference [23], an error function is proposed

$$f_{\text{loss}} = \sum_{i=0}^{M-1} (\tau_{i+1} - \tau_i)^2. \quad (11)$$

Then, there is no matrix calculation in reference [23]. However, there are dividers in the equation (14) of reference [22] and equation (22) of reference [23]. Therefore, it is necessary to propose a new calibration technique without dividers and matrix calculations.

By employing equation (7) to compute $\sum_{j=0}^i (\tau_{j+1} - \tau_j)$,

there is

$$\tau_{i+1} - \tau_0 \approx \frac{\sum_{k=0}^i \sum_{n=1}^L |\Delta y_k[n]| - (i+1)\Delta}{\nabla}. \quad (12)$$

If $\tau_0 = 0$, equation (12) can be rewritten as

$$\tau_{i+1} \approx \frac{\sum_{k=0}^i \sum_{n=1}^L |\Delta y_k[n]| - (i+1)\Delta}{\nabla}. \quad (13)$$

According to equation (13), there is:

$$e_{i+1} = \frac{\sum_{k=0}^i \sum_{n=1}^L |\Delta y_k[n]| - (i+1)\Delta}{\nabla} - \hat{\tau}_{i+1}. \quad (14)$$

Based on equation (14), the iterative algorithm can be represented as:

$$\begin{aligned} \tau_{i+1}[o+1] &= \frac{u_0 \left(\sum_{k=0}^i \sum_{n=1}^L |\Delta \hat{y}_k[n]| - (i+1)\hat{\Delta} \right)}{\hat{\nabla}} + \\ &\quad \tau_{i+1}[o]. \end{aligned} \quad (15)$$

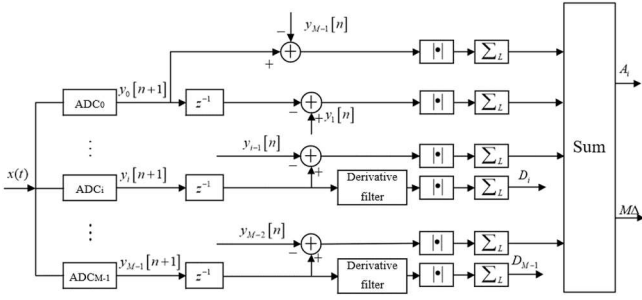


FIGURE 2. Preprocessing model for estimating time skew.

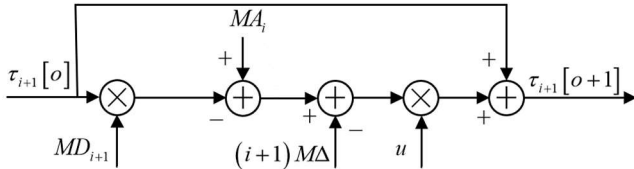


FIGURE 3. Iterative estimation model for time skew.

Here are:

$$\sum_{k=0}^i \sum_{n=1}^L |\Delta \hat{y}_k[n]| = \sum_{k=0}^i \sum_{n=1}^L |\hat{y}_{k+1}[n] - \hat{y}_k[n]|, \quad (16)$$

$$\hat{\Delta} = \frac{\sum_{k=0}^{M-2} \sum_{n=1}^L |\Delta \hat{y}_k[n]| + \sum_{n=1}^L |\hat{y}_0[n+1] - \hat{y}_{M-1}[n]|}{M}, \quad (17)$$

$$\hat{\nabla} = \frac{\sum_{k=0}^{M-1} \sum_{n=1}^L |\hat{y}'_k[n]|}{M}, \quad (18)$$

$$\hat{y}_k[n] = y_k[n] - \tau_k[o] y'_k[n], \quad (19)$$

Additionally, $u_0 \in (0, 2)$. The iterative estimation algorithm for time skew is given in equation (15). When a small iterative step size is taken to ensure algorithm stability, there are many iterations. During each iteration, it is necessary to calculate a large number of calibrated signals and the values in equations (16), (17), and (18). Therefore, the estimation method proposed in equation (15) has a large number of iterations and requires a significant amount of computation during each iteration. As a result, reducing computational complexity during each iteration has significant practical application value.

If the input signal can be linearly approximated, there are [21]:

$$\lim_{N \rightarrow \infty} \sum_{n=1}^N |\Delta y_i[n]| \approx \lim_{N \rightarrow \infty} \sum_{n=1}^N |y'_i[n]| (T_s + \tau_{i+1} - \tau_i), \quad (20)$$

$$\nabla \approx \hat{\nabla}. \quad (21)$$

When L is enough large, according to equation (20) and (21) there is:

$$\sum_{n=1}^L |\Delta \hat{y}_i[n]| \approx \sum_{n=1}^L (|y_{i+1}[n] - y_i[n]| - (\hat{\tau}_{i+1} |y'_{i+1}[n]| - \hat{\tau}_i |y'_i[n]|)). \quad (22)$$

By substituting equations (21) and (22) into equations (16), (17), and (18), there are:

$$\begin{aligned} & \sum_{k=0}^i \sum_{n=1}^L |\Delta \hat{y}_k[n]| \\ & \approx \sum_{i=0}^k \sum_{n=1}^L |\Delta y_{i+1}[n]| - \tau_{k+1}(o) \sum_{n=1}^L |\nabla y_{k+1}[n]| \\ & + \tau_0(o) \sum_{n=1}^L |\nabla y_0[n]| \end{aligned} \quad (23)$$

$$\begin{aligned} & = \sum_{i=0}^k \sum_{n=1}^L |\Delta y_{i+1}[n]| - \tau_{k+1}(o) \sum_{n=1}^L |\nabla y_{k+1}[n]|, \\ & \hat{\Delta} = \frac{\sum_{k=0}^{M-2} \sum_{n=1}^L |\Delta \hat{y}_k[n]| + \sum_{n=1}^L |\hat{y}_0[n+1] - \hat{y}_{M-1}[n]|}{M} \\ & \approx \frac{\sum_{i=0}^{M-2} \sum_{n=1}^L |\Delta y_i[n]| + \sum_{n=1}^L |y_0[n+1] - y_{M-1}[n]|}{M}, \end{aligned} \quad (24)$$

$$\begin{aligned} \hat{\nabla} & = \frac{\sum_{k=0}^{M-1} \sum_{n=1}^L |\hat{y}'_k[n]|}{M} \\ & \approx \frac{\sum_{i=0}^{M-1} \sum_{n=1}^L |y'_i[n]|}{M}. \end{aligned} \quad (25)$$

Substitute equations (23), (24), and (25) into equation (15), there is:

$$\begin{aligned} \tau_{i+1}[o+1] & = \tau_{i+1}[o] + u_1 \left(\sum_{k=0}^i \sum_{n=1}^L |\Delta y_k[n]| \right. \\ & \quad \left. - (i+1)\Delta - \tau_{i+1}[o] \sum_{n=1}^L |y'_{i+1}[n]| \right). \end{aligned} \quad (26)$$

Here $u_1 \in (0, 2/\nabla)$.

Equation (26) demonstrates that by utilizing the principle of linear approximation, it is possible to eliminate the need for recalculating equations (16), (17), and (18) during the iterative process. This significantly reduces the computational resources required for each iteration. However, there is division operation to compute the value of Δ . By substituting $u = u_1 / M$ into equation (26), there is:

$$\begin{aligned} \tau_{i+1}[o+1] & = \tau_{i+1}[o] + (uMA_{i+1} \\ & \quad - (i+1)u(M\Delta) - uM\tau_{i+1}[o]D_{i+1}). \end{aligned} \quad (27)$$

Here, $A_{i+1} = \sum_{k=0}^i \sum_{n=1}^L |\Delta y_k[n]|$, $D_{i+1} = \sum_{n=1}^L |y'_{i+1}[n]|$. Before performing the iteration of equation (27), the values of A_{i+1} , D_{i+1} and $M\Delta$ can be obtained through the module depicted in Fig. 2. Subsequently, their values are utilized as inputs for the iterative module in Fig.3.

Notably, Fig. 2 and Fig. 3 illustrate that the proposed algorithm achieves independence between the number of derivate calculations and the step size factor, without resorting to division operations. This is a significant

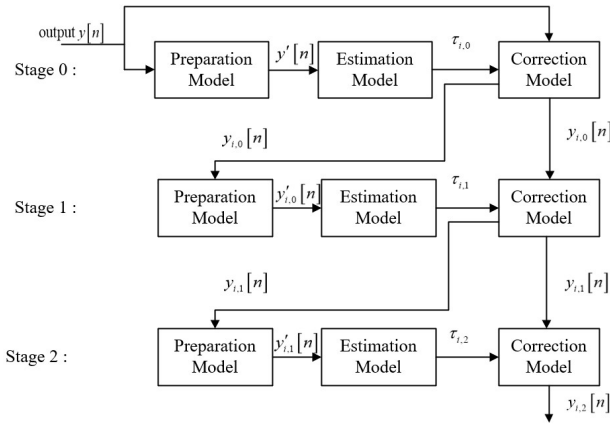


FIGURE 4. The feedback calibration process of the first three stages of a multi-stage feedback.

advantage that is not present in the referenced works [20], [22-24], and [27-29], highlighting the uniqueness and efficiency of our algorithm. The algorithm eliminates the need to calibrate the output signal during each iteration. As a result, the computational complexity in the iterative part of the algorithm is reduced.

B. TIME SKEW CALIBRATION BASED ON IMPROVED MULTI-STAGE FEEDBACK

When the time skew is large, the Taylor series approximation error also increases. To reduce the impact of Taylor series approximation error on calibration results, a multi-step feedback calibration algorithm has been proposed. In Fig. 4, the calibration process of the first three stages of multi-stage feedback is presented. This method estimates the residual time skew after calibration based on the output calibrated at the previous stage. By estimating the residual time skew multiple times, the time skew estimation accuracy is improved. Where $y_{i,0}[n]$, $y_{i,1}[n]$ and $y_{i,2}[n]$ represent the estimated time skew in Stage 0, Stage 1, and Stage 2, respectively. Moreover, $\tau_{i,0}$, $\tau_{i,1}$, and $\tau_{i,2}$ represent the estimated time skew in Stage 0, Stage 1, and Stage 2, respectively.

The calibrated output signals in Stage 0, Stage 1, and Stage 2 are represented as follows:

$$y_{i,0}[n] = y_i[n] - \tau_{i,0}y'_i[n], \quad (28)$$

$$y_{i,1}[n] = y_{i,0}[n] - \tau_{i,1}y'_{i,0}[n], \quad (29)$$

$$y_{i,2}[n] = y_{i,1}[n] - \tau_{i,2}y'_{i,1}[n]. \quad (30)$$

In Stage 0, the time skew is iteratively estimated by the estimation module using the algorithm described in Section III-A, while some invariant parameters during the iteration are calculated by the preparation module. Then, preliminary corrections are made to the output signal by the correction module using these estimated time skews.

After Stage 0, the time skew is significantly reduced.

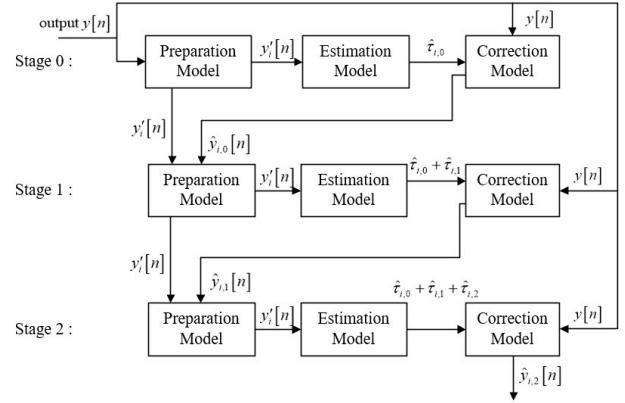


FIGURE 5. The feedback calibration process of the first three stages of an improved multi-stage feedback

Nevertheless, a non-negligible time skew persists due to the Taylor series approximation.

In Stage 1, the estimation module is employed again, this time to approximately estimate the remaining time skew in the signal corrected in Stage 0. Because the time skew has been reduced, the estimation accuracy is higher than at the previous stage.

Finally, in Stage 2, the signal undergoes correction by the correction module, utilizing the more precise time mismatch error estimated in Stage 1.

Through this multi-step feedback structure, the errors stemming from the Taylor series approximation are gradually minimized, thereby enhancing the overall calibration accuracy and precision.

Based on equations (28), (29), and (30), the relationship between the final output after the initial three-step calibration of the multi-step feedback algorithm and the signal before calibration is as follows:

$$y_{i,2}[n] = y_i[n] - (\tau_{i,0} + \tau_{i,1} + \tau_{i,2})y'_i[n] + (\tau_{i,0}\tau_{i,1} + \tau_{i,0}\tau_{i,2} + \tau_{i,1}\tau_{i,2})y''_i[n] - \tau_{i,0}\tau_{i,1}\tau_{i,2}y'''_i[n]. \quad (31)$$

According to equation (31), the final output after calibration by the P-stage feedback can be expressed as

$$y_{i,P-1}[n] = y_i[n] - \sum_{k=1}^P c_k y^{(k)}_i[n]. \quad (32)$$

Where c_k is the function of the estimated time skew τ_q ($q = 0, 1, \dots, P-1$). Equation (32) indicates that for a P-stage feedback algorithm, each sample requires P derivative calculations. To address this, Fig. 5 illustrates a feedback calibration process of the first three stages of improved multi-stage feedback. The improved multi-stage feedback aims to reduce derivative calculations. Where $\hat{y}_{i,0}[n]$, $\hat{y}_{i,1}[n]$ and $\hat{y}_{i,2}[n]$ represent the estimated time skew in Stage 0, Stage 1, and Stage 2, respectively. Moreover, $\hat{\tau}_{i,0}$, $\hat{\tau}_{i,1}$, and $\hat{\tau}_{i,2}$ represent the estimated time skew in Stage 0,

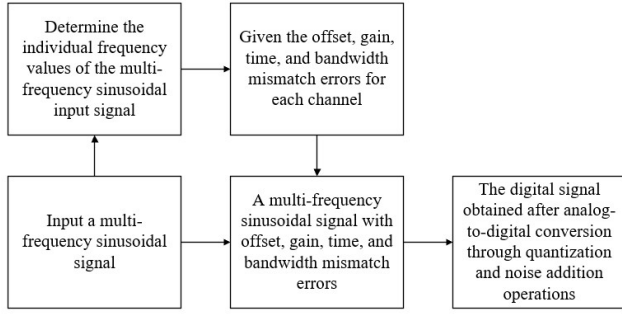


FIGURE 6. Constructing process of a time-interleaved sampling system in MATLAB.

Stage 1, and Stage 2, respectively.

In Fig. 5, after estimating the residual time skew from the previous stage, the derivative of the original output $y_i[n]$, is used to calibrate the output signal in each stage. The calibrated output at Stage 0, Stage 1, and Stage 2 can be expressed as follows:

$$\hat{y}_{i,0}[n] = y_i[n] - \hat{\tau}_{i,0} y'_i[n], \quad (33)$$

$$\hat{y}_{i,1}[n] = \hat{y}_{i,0}[n] - \hat{\tau}_{i,1} y'_{i,0}[n], \quad (34)$$

$$\hat{y}_{i,2}[n] = \hat{y}_{i,1}[n] - \hat{\tau}_{i,2} y'_{i,1}[n]. \quad (35)$$

According to equations (33), (34) and (35), the final output from the improved P-stage feedback can be expressed as:

$$\hat{y}_{i,P-1}[n] = y_i[n] - \sum_{p=0}^{P-1} \hat{\tau}_{i,p} y'_i[n]. \quad (36)$$

Compared with equation (32), equation (36) reduces the number of derivative calculations required for each sample point from P times to just one time. Moreover, according to equation (32) and (36), if $\tau_{i,p} \approx \hat{\tau}_{i,p}$, the improved multi-stage feedback algorithm can achieve the same time skew estimation results as the multi-level Taylor series calibration of Fig. 4. Therefore, we will prove that $\tau_{i,p} \approx \hat{\tau}_{i,p}$.

Since both $\tau_{i,0}$, $\hat{\tau}_{i,0}$, $\tau_{i,1}$ and $\hat{\tau}_{i,1}$ are time skews estimated by the first derivative of the output signal and the algorithm in Section III-A, there are $\tau_{i,0} = \hat{\tau}_{i,0}$ and $\tau_{i,1} = \hat{\tau}_{i,1}$. However, the relationship between $\tau_{i,2}$ and $\hat{\tau}_{i,2}$ remains unknown. According to equation (13), when the iterative algorithms converge, the values of $\tau_{i+1,2}$ and $\hat{\tau}_{i+1,2}$ can be expressed as:

$$\tau_{i+1,2} \approx \frac{M \sum_{k=0}^i \sum_{n=1}^L |\Delta y_{k,1}[n]| - \sum_{i=0}^{M-2} \sum_{n=1}^L |\Delta y_{i,1}[n]|}{\sum_{i=0}^{M-1} \sum_{n=1}^L |y'_{i,1}[n]|} - \frac{\sum_{n=1}^L |y_{0,1}[n+1] - y_{M-1,1}[n]|}{\sum_{i=0}^{M-1} \sum_{n=1}^L |y'_{i,1}[n]|}. \quad (37)$$

$$\hat{\tau}_{i+1,2} \approx \frac{M \sum_{k=0}^i \sum_{n=1}^L |\Delta \hat{y}_{k,1}[n]| - \sum_{i=0}^{M-2} \sum_{n=1}^L |\Delta \hat{y}_{i,1}[n]|}{\sum_{i=0}^{M-1} \sum_{n=1}^L |\hat{y}'_{i,1}[n]|} - \frac{\sum_{n=1}^L |\hat{y}_{0,1}[n+1] - \hat{y}_{M-1,1}[n]|}{\sum_{i=0}^{M-1} \sum_{n=1}^L |\hat{y}'_{i,1}[n]|}. \quad (38)$$

According to equations (28) and (29), $\sum_{n=1}^L |\Delta y_{i,1}[n]|$ can be represented as:

$$\sum_{n=1}^L |\Delta y_{i,1}[n]| = \sum_{n=1}^L |y_{i+1,0}[n] - \tau_{i+1,1} y'_{i+1,0}[n] - y_{i,0}[n] + \tau_{i,1} y'_{i,0}[n]| \quad (39)$$

Substituting equation (22) into equation (39) yields:

$$\sum_{n=1}^L |\Delta y_{i,1}[n]| \approx \sum_{n=1}^L |y_{i+1,0}[n] - y_{i,0}[n]| + \tau_{i+1,1} \sum_{n=1}^L |y'_{i,0}[n]| - \tau_{i,1} \sum_{n=1}^L |y'_{i+1,0}[n]| \quad (40)$$

Substituting equation (40) into equation (37) yields:

$$\tau_{i+1,2} \approx \frac{M \left(\sum_{k=0}^i \sum_{n=1}^L |\Delta y_{k,0}[n]| - \tau_{i+1,1} \sum_{n=1}^L |y'_{i+1,0}[n]| \right)}{\sum_{i=0}^{M-1} \sum_{n=1}^L |y'_{i,1}[n]|} - \frac{\sum_{i=0}^{M-2} \sum_{n=1}^L |\Delta y_{i,0}[n]| + \sum_{n=1}^L |y_{0,0}[n+1] - y_{M-1,0}[n]|}{\sum_{i=0}^{M-1} \sum_{n=1}^L |y'_{i,1}[n]|}. \quad (41)$$

After obtaining $\sum_{n=1}^L |\Delta \hat{y}_{i,1}[n]|$ using the method in equation (40), the expression for $\hat{\tau}_{i+1,2}$ is given by:

$$\hat{\tau}_{i+1,2} \approx \frac{M \left(\sum_{k=0}^i \sum_{n=1}^L |\Delta \hat{y}_{k,0}[n]| - \hat{\tau}_{i+1,1} \sum_{n=1}^L |\hat{y}'_{i+1,0}[n]| \right)}{\sum_{i=0}^{M-1} \sum_{n=1}^L |\hat{y}'_{i,1}[n]|} - \frac{\sum_{i=0}^{M-2} \sum_{n=1}^L |\Delta \hat{y}_{i,0}[n]| + \sum_{n=1}^L |\hat{y}_{0,0}[n+1] - \hat{y}_{M-1,0}[n]|}{\sum_{i=0}^{M-1} \sum_{n=1}^L |\hat{y}'_{i,1}[n]|}. \quad (42)$$

Since both $y_{i,1}[n]$ and $\hat{y}_{i,1}[n]$ are approximately the delayed signals of the output signal $y_i[n]$, according to equation (21), it follows that:

$$\sum_{n=1}^L |y'_{i+1,0}[n]| = \sum_{n=1}^L |\hat{y}'_{i+1,0}[n]| \quad (43)$$

TABLE II
BASIC PARAMETERS OF THE SIMULATION MODEL

THE NUMBER OF CHANNELS	OFFSET	GAIN	TIME SKEW	THE BANDWIDTH OF THE SAMPLE-AND-HOLD CIRCUIT
1	$o_0 = 0.010A_{\max}$	$g_0 = 1.020$	$\tau_0 = 0.004T_s$	$\omega_0 = 4.021f_s$
2	$o_1 = -0.020A_{\max}$	$g_1 = 1.010$	$\tau_1 = -0.007T_s$	$\omega_1 = 4.032f_s$
3	$o_2 = -0.040A_{\max}$	$g_2 = 0.990$	$\tau_2 = 0.009T_s$	$\omega_2 = 3.970f_s$
4	$o_3 = 0.030A_{\max}$	$g_3 = 1.010$	$\tau_3 = -0.003T_s$	$\omega_3 = 4.011f_s$

A_{\max} represents the maximum amplitude of the input signal, T_s represents the sampling period of the sampling system, f_s represents the sampling frequency of the sampling system.

$$\sum_{i=0}^{M-1} \sum_{n=1}^L |y'_{i,1}[n]| = \sum_{i=0}^{M-1} \sum_{n=1}^L |\hat{y}'_{i,1}[n]| \quad (44)$$

Due to $\tau_{i+1,1} = \hat{\tau}_{i+1,1}$ and $y_{i,0}[n] = \hat{y}_{i,0}[n]$, according to equations (41) and (42), it is obtained that $\tau_{i+1,2} \approx \hat{\tau}_{i+1,2}$.

According to equation (13), when the iterative algorithms converge, the values of $\tau_{i+1,p}$ and $\hat{\tau}_{i+1,p}$ can be expressed as:

$$\tau_{i+1,p} \approx \frac{M \sum_{k=0}^i \sum_{n=1}^L |\Delta y_{k,p-1}[n]| - \sum_{i=0}^{M-2} \sum_{n=1}^L |\Delta y_{i,p-1}[n]|}{\sum_{i=0}^{M-1} \sum_{n=1}^L |y'_{i,p-1}[n]|} \quad (45)$$

$$\hat{\tau}_{i+1,p} \approx \frac{\sum_{n=1}^L |y_{0,p-1}[n+1] - y_{M-1,p-1}[n]|}{\sum_{i=0}^{M-1} \sum_{n=1}^L |y'_{i,p-1}[n]|} \cdot \frac{M \sum_{k=0}^i \sum_{n=1}^L |\Delta \hat{y}_{k,p-1}[n]| - \sum_{i=0}^{M-2} \sum_{n=1}^L |\Delta \hat{y}_{i,p-1}[n]|}{\sum_{i=0}^{M-1} \sum_{n=1}^L |\hat{y}'_{i,p-1}[n]|} \quad (46)$$

According to equations (40), there are

$$\sum_{n=1}^L |\Delta y_{i,p-1}[n]| \approx \sum_{n=1}^L |\Delta y_{i,p-2}[n]| + \tau_{i,p-1} \sum_{n=1}^L |y'_{i,p-2}[n]| - \tau_{i+1,p-1} \sum_{n=1}^L |y'_{i+1,p-2}[n]|. \quad (47)$$

$$\sum_{n=1}^L |\Delta \hat{y}_{i,p-1}[n]| \approx \sum_{n=1}^L |\Delta \hat{y}_{i,p-2}[n]| + \hat{\tau}_{i,p-1} \sum_{n=1}^L |\hat{y}'_{i,p-2}[n]| - \hat{\tau}_{i+1,p-1} \sum_{n=1}^L |\hat{y}'_{i+1,p-2}[n]|. \quad (48)$$

According to equation (21), there is

$$\sum_{n=1}^L |y'_{i+1,p-2}[n]| \approx \sum_{n=1}^L |\hat{y}'_{i+1,p-2}[n]| \quad (49)$$

Based on equations (45) to (49), when the estimated time

skew are $\tau_{i+1,p-1} \approx \hat{\tau}_{i+1,p-1}$ and

$\sum_{n=1}^L |\Delta y_{i,p-2}[n]| \approx \sum_{n=1}^L |\Delta \hat{y}_{i,p-2}[n]|$, there are $\tau_{i+1,p} \approx \hat{\tau}_{i+1,p}$ and

$\sum_{n=1}^L |\Delta y_{i,p-1}[n]| \approx \sum_{n=1}^L |\Delta \hat{y}_{i,p-1}[n]|$. Since the iteration

environment was the same for the first time, there are

$\tau_{i+1,0} = \hat{\tau}_{i+1,0}$ and $\sum_{n=1}^L |\Delta y_{i,0}[n]| = \sum_{n=1}^L |\Delta \hat{y}_{i,0}[n]|$. Therefore,

there is $\tau_{i+1,p} \approx \hat{\tau}_{i+1,p}$.

As a result, the estimation time skew of the improved P-stage feedback algorithm is equivalent to the time skew estimated by a P-order Taylor series expansion approximation. Therefore, the improved P-order feedback algorithm can effectively reduce the approximation error caused by Taylor series expansion without increasing the number of derivatives. For an M -channel TI-ADC system, the proposed improved algorithm only requires $(M-1)L$ derivations.

IV. SIMULATION RESULTS

In this Section, a 4-channel 12-bit TI-ADCs model is constructed in MATLAB. The entire construction process is shown in Fig. 6. According to the analysis of mismatches in time-interleaved sampling systems [4], the first step is to determine the amplitude, phase, and frequency values of each sinusoidal component within the input multi-frequency signal. Secondly, based on the predefined values of offset, gain, time skew, and bandwidth mismatch, as well as the frequency values of the input signal, the amplitudes and phases of the sinusoidal signals are adjusted. This process results in signals with multiple frequencies within the time-interleaved sampling system that exhibit offset, gain, time skew, and bandwidth mismatch. Finally, quantization and noise addition operations are performed to simulate a time-interleaved sampling system with quantization noise, additive noise, offset, gain, time skew, and bandwidth mismatch. Owing to the presence of Gaussian white noise, the SNR of each channel is maintained at 80dB. As presented in TABLE II, the values of mismatches within the system are detailed. All simulations presented in this section are based

TABLE III
MAXIMUM BANDWIDTH VALUES FOR DIFFERENT NUMBER OF TAPS

Number of Taps	11	13	15	17	19	21	23	25	27	29	31	33	35	37
Normalized Maximum Bandwidth Value	0.268	0.309	0.338	0.359	0.375	0.388	0.398	0.407	0.414	0.421	0.426	0.431	0.435	0.439

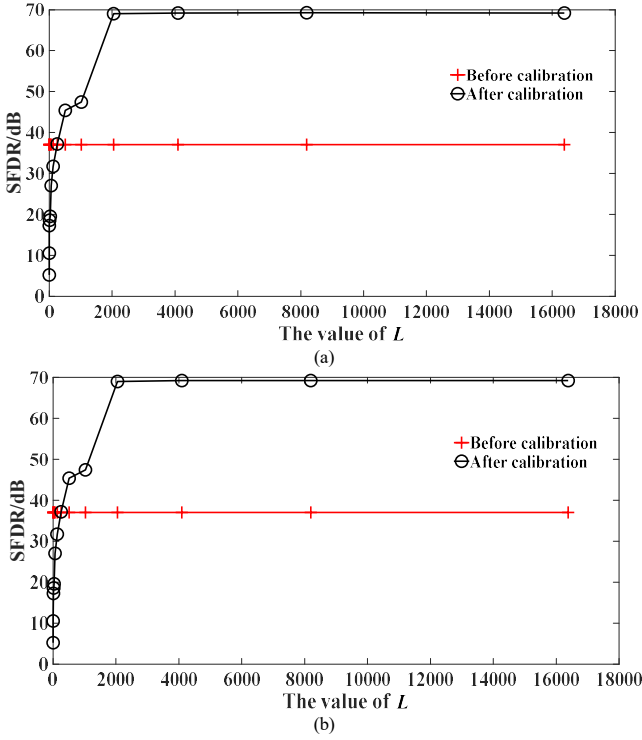


FIGURE 7. The performance of the TI-ADCs with the different values of L , (a) the SNDR before and after calibration; (b) the SFDR before and after calibration.

on the constructed 4-channel 12-bit TI-ADCs model.

A. MITIGATION STRATEGIES FOR OFFSET, GAIN, AND BANDWIDTH MISMATCH ERRORS

When the input signal does not simultaneously exist at two frequency signals symmetric about $\frac{k}{2}f_c$ (k is a positive integer), the offset and gain can be estimated by

$$o_i = \frac{\sum_{n=1}^L y_i[n]}{L}, \quad (50)$$

$$g_i = \sqrt{\frac{\sum_{n=1}^L (y_i^2[n])}{L-1}}. \quad (51)$$

In relation to time skew and bandwidth mismatch, the frequency response function of the system is detailed in [9]:

$$H_{\Delta\tau_i, \Delta\omega_i}(j\omega) = e^{j\omega\tau} \times \frac{1 + j\frac{\omega}{\omega_{bi}}}{1 + j\frac{\omega}{\omega_{bo}}}. \quad (52)$$

Transforming the form of equation (52) can yield:

$$H_{\Delta\tau_i, \Delta\omega_i}(j\omega) \approx e^{j\omega(\tau_i - \tau_0)} \times \left(1 + j\omega \left(\frac{1}{\omega_{bi}} - \frac{1}{\omega_{br}} \right) - (j\omega)^2 \left(\frac{1}{\omega_{bi}^2} - \frac{1}{\omega_{br}^2} \right) \right). \quad (53)$$

Based on equation (53), bandwidth mismatch mainly leads to frequency-dependent phase mismatch when the sub-ADC bandwidth is much larger than the signal bandwidth. However, when the sub-ADC bandwidth is comparable to the signal bandwidth, bandwidth mismatch can also cause amplitude mismatch. Therefore, the proposed algorithm can be applied to calibrate time skew and bandwidth mismatch when the sub-ADC bandwidth is much larger than the signal bandwidth.

B. DETERMINATION OF IMPORTANT PARAMETERS OF THE PROPOSED TECHNIQUES

For the algorithms proposed in section III, there are two parameters that demand attention, namely the filter's taps [29] and the input signal samples. Next, appropriate parameters are selected via simulations.

The coefficients of the derivative filter $h_d[n]$ can be expressed as

$$h_d[n] = \begin{cases} \cos\left(\frac{n\pi}{2}\right), & (n \neq 0) \\ 0, & (n = 0) \end{cases}, \quad (54)$$

The Blackman window function is used to truncate the coefficients in equation (54) to obtain the FIR filter coefficients of finite length. Therefore, the filter in equation (54) exhibits a linear phase response. However, the number of filter taps has an impact on the amplitude-frequency characteristics of the designed FIR filter. The normalized amplitude fluctuation α is defined as:

$$\alpha = \frac{A_{\omega_N}}{\omega_N} - 1. \quad (55)$$

Where ω_N represents the digital angular frequency, and the amplitude response of the FIR filter at the digital angular frequency ω_N is denoted as A_{ω_N} . The normalized kurtosis fluctuation is defined as:

$$\alpha_{wp} = \max\{|\alpha_w|\}. \quad (56)$$

In this context, $\{|\alpha_w|\}$ represents the collection of

TABLE IV
THE SNDR AND SFDR AFTER FOR THE DIFFERENT VALUE OF L

The value of L	2	4	8	16	32	64	128	256	512	1024	2048	4096	8192	16384
SNDR(dB)	2.07	7.18	14.23	15.52	16.57	23.99	28.70	34.22	42.29	44.52	66.75	66.72	66.77	66.69
SFDR(dB)	5.23	10.52	17.27	18.59	19.57	27.03	31.74	37.20	45.39	47.43	69.28	69.21	69.24	69.21

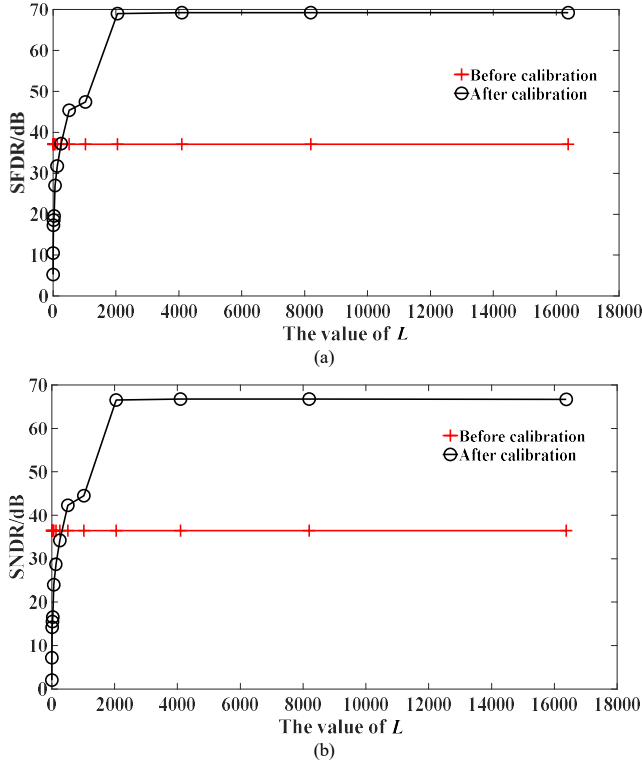


FIGURE 8. The performance of the TI-ADCs with the different values of L , (a) the SNDR before and after calibration; (b) the SFDR before and after calibration.

absolute values of normalized amplitude fluctuations $|\alpha_w|$ at various frequencies within a bandwidth-limited signal.

To ensure that the designed derivative filter exhibits satisfactory performance for band-limited signals, it is necessary for the value of α_{wp} in equation (56) to be sufficiently small. Based on this, when the normalized kurtosis fluctuation is required to be within 0.01, the bandwidth limitations of the input signal under different filter tap counts are presented in TABLE III.

From the perspective of the maximum bandwidth alone, selecting the filter with 37 taps appears to be the optimal choice. However, increasing the number of taps from 11 to 37 results in nearly a fourfold increase in power consumption and mathematical resources required for correcting time skew. Additionally, while the normalized bandwidth value increases by approximately 0.12 when the number of taps increases from 11 to 21, it only improves by about 0.05 when the number of taps increases from 21 to 37.

Therefore, considering both power consumption and bandwidth considerations, it is ultimately decided to adopt a first-order derivative filter with 21 taps and a Blackman

window function as the first-order FIR derivative filter for time skew calibration.

Our statistical knowledge-based calibration method exhibits larger and uncertain errors with insufficient samples. Therefore, selecting an appropriate sample size is a crucial issue. Derivative calculations are performed using digital filters and the interleaved and reorganized output $y[n]$. Therefore, the input signal frequency is constrained within the range of $(0, 0.388f_s]$. Fig. 7 shows the SNDR and SFDR before and after calibration for the different number of samples when the number of filter taps is 21 and the frequency of input is $0.388f_s$. The calibration algorithm adopted is the method proposed in Section III-B. Additionally, TABLE IV presents the calibrated SNDR and SFDR under various values of L . It can be observed that when condition $L \geq 512$ is met, the algorithm begins to exhibit a certain calibration effect. Furthermore, when condition $L \geq 2048$ is satisfied, the calibrated SNDR stabilizes above 66 dB, and the SFDR stabilizes above 69 dB. Therefore, selecting $L = 2048$ is a good choice.

C. VERIFICATION OF THE PROPOSED TIME SKEW CALIBRATION TECHNIQUE

The time skew calibration technique of Section III-A is used to calibrate the four-channel TI-ADCs. The number of samples in each channel is 2048, and μ is 0.00001.

The designed derivative filter was then employed in both the Section III-A and Section III-B calibration methods. The effects of calibration before and after are illustrated in Fig. 8.

When using the Section III-A method for time skew calibration, a significant decrease in calibration effectiveness as the input signal frequency increases. However, when the Section III-B method is employed for time skew calibration, the impact of increasing signal frequency on calibration performance is less pronounced compared to the Section III-A method. This indicates that the method proposed in Section III-B can effectively reduce the impact of Taylor series approximation errors on the calibration results.

As shown in Fig. 8, after calibrating time skew using the combination of Section II-C and Section III-B methods, the calibrated SNDR remains above 66dB, and the SFDR is above 69dB. This result approximately satisfies the requirement for a data acquisition system with an ENOB of 10 bits or higher.

In Fig. 8, the spectrum of a sinusoidal signal with a frequency of approximately $0.388f_s$ is presented before and after calibrating time skew using the method described in

TABLE V
COMPARISON WITH OTHER TECHNIQUES

	[11] work	[22] work	[24] work	[25] work	This work
Number of channels	4	4	4	2	4
Input frequency	Above $0.43f_s$	Above $0.39f_s$	$0.37f_s$	$0.47f_s$	Above $0.39f_s$
Filter tap with estimation time skew	25	21	31	13	21
Derivation	5.00K	3.10K	110.00K	24.50K	6.14K
Divider	1	1	0	0	0
Multiplication	125.00K	65.10K	3410.00K	318.5K	128.94K
SNDR (dB)	Above 61.00	46.00	Above 69.00	48.50	66.75
SFDR (dB)	Above 89.00	Above 51.00	Above 71.00	56.60	69.28

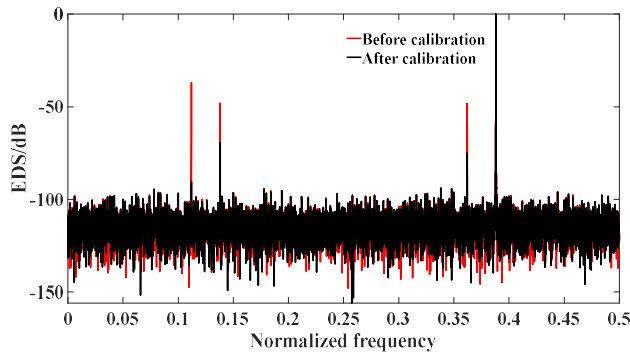


FIGURE 9. The spectrogram before and after calibration of a sinusoidal signal with a frequency of $0.388f_s$.

Section III-B. For the high-frequency sinusoidal signal shown in Fig. 8, the SNDR before calibration is 36.43dB, and the SFDR is 37.06dB. After calibration, the SNDR improves to 66.75dB, and the SFDR rises to 69.28dB. As can be seen from Fig. 8, the proposed algorithm still exhibits a satisfactory calibration effect for high-frequency sinusoidal input signals.

Fig. 9 presents the estimated time skew values obtained by the calibration algorithm in Fig. 8 as the number of steps increases. These error values represent the time skew of each channel relative to Channel 0. Therefore, the default time skew for channel 0 is zero, and thus calibration for time skew is not necessary for channel 0.

From Fig. 10 (a), it can be observed that after 16 steps (80k times), the estimated relative time skew values for Channels 1, 2, and 3 are approximately $-0.0111T_s$, $0.0048T_s$, and $-0.0073T_s$, respectively. The difference between these estimated values and the error values set in TABLE II is minimal. The slight deviation is mainly due to the approximation error resulting from the Taylor series expansion. As can be seen from Fig. 10(b), after stable convergence, the SNDR is above 65dB, the SFDR is above 69dB. This signifies that a minor deviation between the estimated and actual errors is permissible.

TABLE V compares the calibration performance of this work with previous works [11], [22], [24], and [25] in terms of the calibration effect on a single sinusoidal signal. The

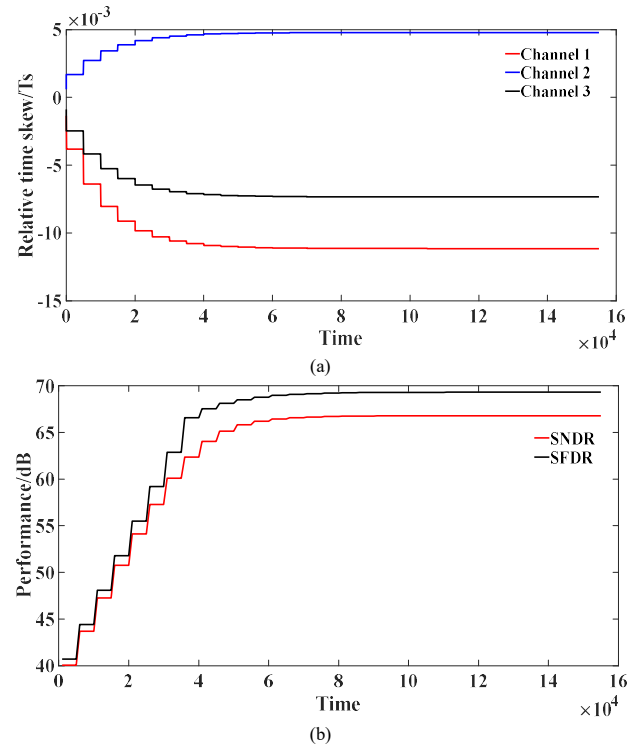


FIGURE 10. Convergence curves of Fig. 9, (a) Relative time skew; (b) SNDR and SFDR.

data for this work is derived from the performance display of the frequency of $0.388f_s$ in Fig. 9.

In reference [25], the algorithm is capable of calibrating time skew in the system with fewer filter taps. However, it is the only algorithm in the table that has a limit on the number of channels, indicating its weaker generality compared to other algorithms. When comparing the usage of derivatives, we observe that the algorithms in references [11] and [22] require significantly fewer derivatives than those in references [24] and [25]. Nevertheless, achieving an extremely low number of derivatives often necessitates the introduction of division modules.

The method proposed in this paper achieves a low-complexity algorithm without the need for division by employing a slightly higher number of derivatives compared

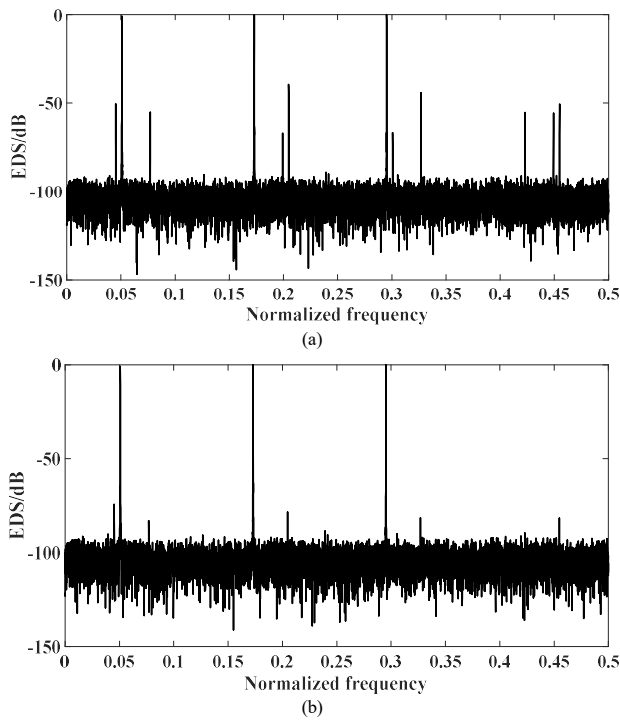


FIGURE 11. The performance of the wideband multi-tone sinusoidal signal, (a) before calibration; (b) after calibration.

to references [11] and [22]. The use of a multi-step feedback mechanism significantly enhances the calibration performance of the proposed algorithm for high-frequency signals compared to reference [22]. Specifically, at an input signal of approximately 0.39fs, the signal-to-noise-and-distortion ratio (SNDR) achieved by the calibration in this paper is 20.75dB higher than that in reference [22]. This demonstrates that the proposed method not only maintains a low derivative complexity but also significantly improves calibration performance, especially for high-frequency signal processing.

Furthermore, when compared to the algorithms presented in references [22], [24], and [25], the algorithm proposed in this paper consumes the least number of multiplications, all without division operations.

To demonstrate the ability of the proposed method to calibrate complex input signals, Fig. 11 and Fig. 12 present the frequency spectra of a multi-tone sinusoidal signal and a frequency modulation signal, respectively, before and after calibration. In Fig. 11, the SNDR and SFDR of the multi-tone sinusoidal signal before calibration are 42.20dB and 39.45dB, respectively. However, after calibration, the SNDR increases to 67.01dB, and the SFDR rises to 74.30dB. This significant improvement in both SNDR and SFDR validates the effectiveness of the calibration process. Fig. 12 depicts the frequency spectra of the frequency modulation signal before and after calibration. Before calibration, the SFDR is 47.94dB, but it improves to 72.66dB after calibration. As evident in Fig. 11 and Fig. 12, the large spurious signals resulting from time skew are effectively suppressed after

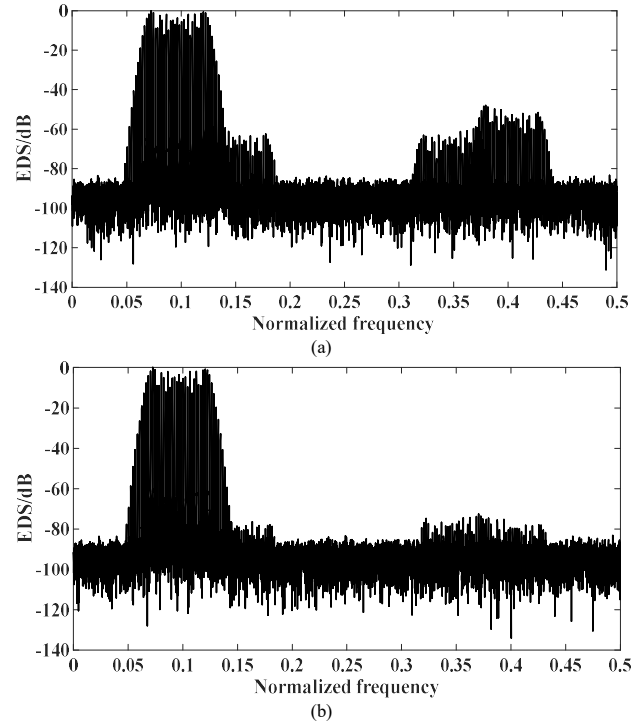


FIGURE 12. The performance of the wideband multi-tone sinusoidal signal, (a) before calibration; (b) after calibration.

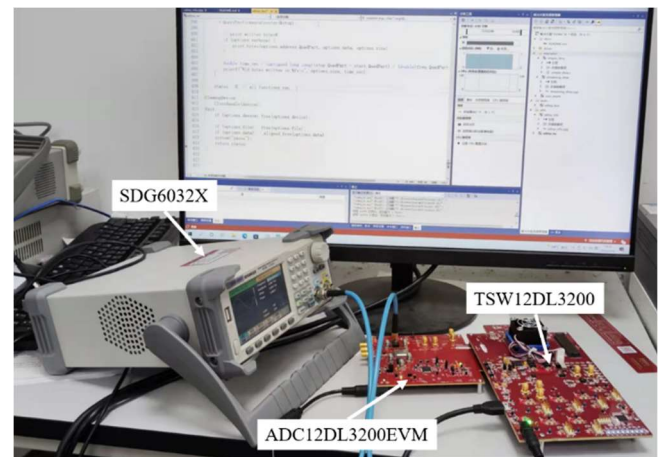


FIGURE 13. A 2-channel 12-bit 6.4Gbps TI-ADCs.

calibration. This underscores the capability of the proposed algorithm to calibrate complex input signals.

V. EXPERIMENTAL RESULTS

A. THE ACQUISITION OF EXPERIMENTAL DATA

Fig. 13 shows a 2-channel 12-bit 6.4Gbps TI-ADCs. And the TI-ADCs consists of three parts: a). Arbitrary waveform generator (SDG6032X), b). analog-to-digital conversion system (ADC12DL3200EVM), c). data capture card (TSW12DL3200EVM).

Fig. 14 demonstrates the operational mechanism of the TI-

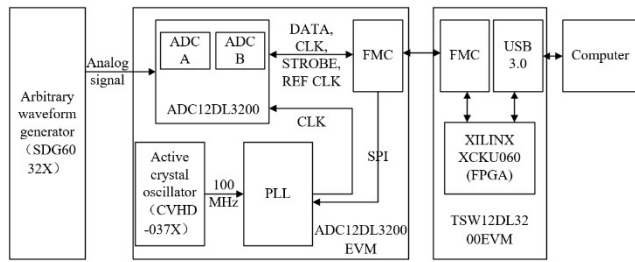


FIGURE 14. The schematic diagram of the TI-ADCs.

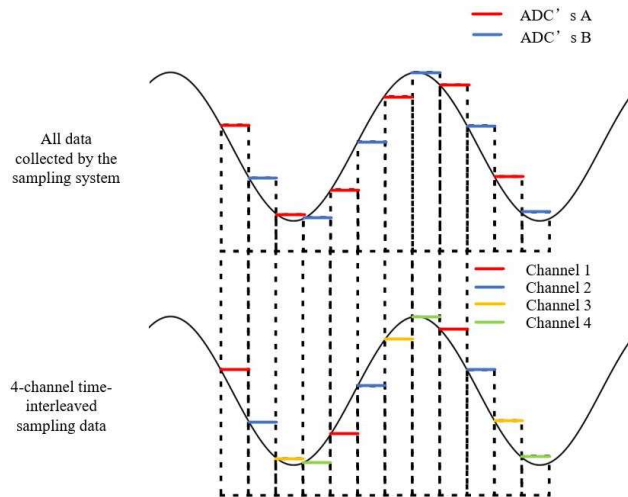


FIGURE 15. A 4-channel time-interleaved sampling data obtained by the sampling system in Fig. 13.

ADCs. Initially, an analog signal is generated using an arbitrary waveform generator. Subsequently, the ADC12DL3200EVM and TSW12DL3200EVM are configured using a computer by writing to their respective registers. These register configurations ensure the proper functioning of the overall system. Once the configurations are complete, the active crystal oscillator and phase-locked loop are employed to generate the sampling clock for the ADC. The ADC's A and B modules then perform time-interleaved sampling at different sampling clocks. Finally, the sampled data is transmitted to the TSW12DL3200EVM via the FMC, and from there, it is sent to the computer via USB 3.0.

B. IMPLEMENTATION BASED ON VIVADO

The pre-calibration data of the dual-channel time-interleaved system can be obtained from Section V-A. However, the simulation was conducted in a 4-channel system, which may be confusing. For clarity, the collected dual-channel data can be split into a 4-channel system. Specifically, channels 1 and 3 are derived from the odd and even columns of the data collected by ADC's A, respectively. Similarly, channels 2 and 4 are derived from the odd and even columns of the data collected by ADC's B, respectively.

In Fig. 15, it is shown how data collected from two ADCs

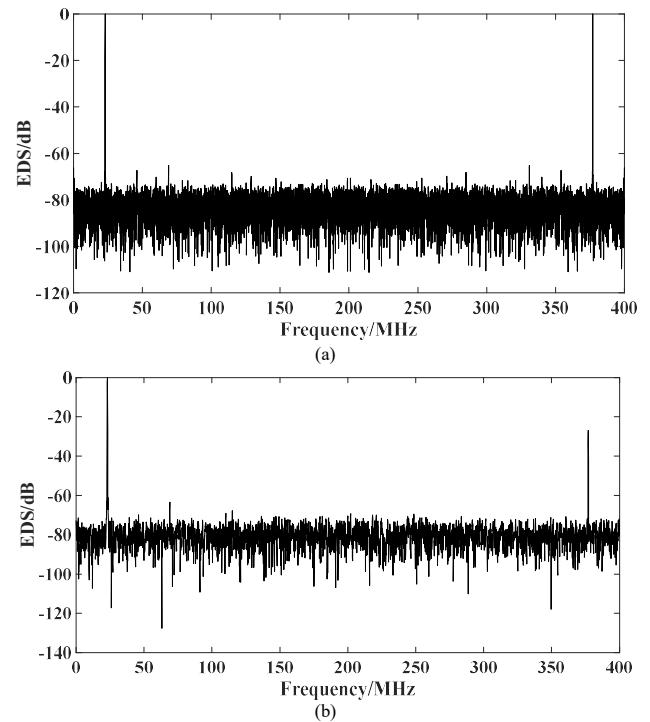


FIGURE 16. The frequency spectra before and after calibrating offset and gain: (a) the frequency spectrum before calibration; (b) the frequency spectrum after calibration.

on the development board can be transformed into four channels. As can be seen in Fig. 15, the data for Channels 1 and 3 comes from ADCA, while the data for Channels 2 and 4 comes from ADCB. Therefore, Channels 1 and 3 share the same mismatches, and Channels 2 and 4 share the same mismatches. However, due to the differences between the ADCA and ADCB devices, there are distinct mismatches between Channels 1 and 2, as well as between Channels 3 and 4. Consequently, by transforming the data into four channels, it is possible to simulate the data collected by 4-channel TI-ADCs. In this simulated system, Channels 1 and 3 exhibit the same mismatches, while Channels 2 and 4 exhibit the same mismatches.

A sinusoidal signal is generated by the SDG6032X. It has a peak-to-peak voltage of 0.30V and a frequency of 23MHz. Subsequently, this signal is converted from an analog signal to a digital signal in the ADC12DL3200EVM. The actual sampling rate of TI-ADCs is set to 800Msps.

After calibrating the offset and gain using the method described in Section IV-A, the frequency spectra before and after calibration are shown in Fig. 16.

In Fig. 16, following the calibration of the offset and gain, the SNDR is 26.83 dB, and the SFDR is 26.90 dB. This result suggests that there may be a considerable time skew in the system

When the time skew is too large, the Taylor series approximation can introduce significant calculation errors, which may cause the proposed algorithm to fail. We use the fractional delay filter proposed in [9] to make an initial

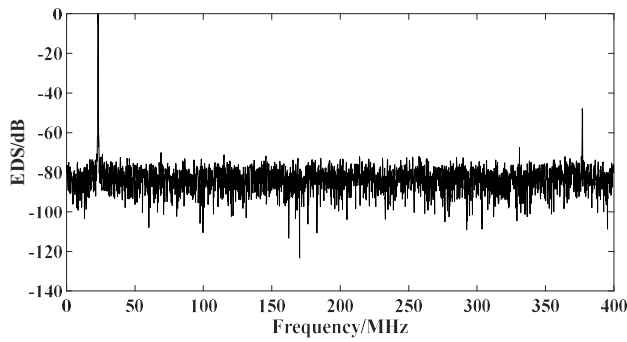


FIGURE 17. The frequency spectrum after rough calibration of time skew.

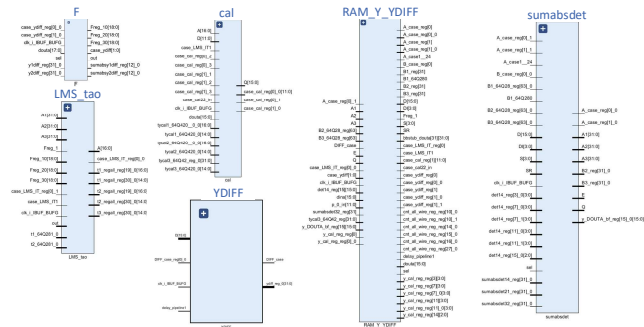


FIGURE 18. The modules required for implementing the algorithm in Section III-B in Vivado.

estimation of the time skew in the system. By gradually approximating the true time skew in the system using delay coefficients rounded to 4 decimal places, we found that when the delay coefficient for Channels 2 and 4 is set to 0.9555, the system's SNDR and SFDR perform relatively well. Fig. 17 shows the frequency spectrum of the signal after coarse calibration. In Fig. 17, the SNDR after calibration is 44.72 dB, and the SFDR is 47.91 dB. However, this result indicates that the SFDR of the system is still relatively low after coarse calibration. Therefore, the signal after coarse calibration is imported into Vivado, where the proposed calibration algorithm is used to fine-tune the time skew.

All field programmable gate array (FPGA) verification is based on the chip XC7vx485tffg1157-1. The data used for verification are derived from Fig. 17.

Fig. 18 demonstrates the modules required for implementing the algorithm in Section III-B in Vivado. The "YDIFF" module is used to calculate the derivative of the input signal, while the "RAM_Y_YDIFF" module stores both the input signal and its derivative in RAM. The "sumabsdet" module calculates the value of A_i in Fig. 3, and the "F" module computes the value of D_i in Fig. 3. The "LMS_tao" module performs iterative calculations to determine the time skew, and the "cal" module implements the calibration of the input signal. Through the modules presented in Fig. 18, the calibration algorithm proposed in Fig. 2, Fig. 3, and Fig. 5 can be achieved.

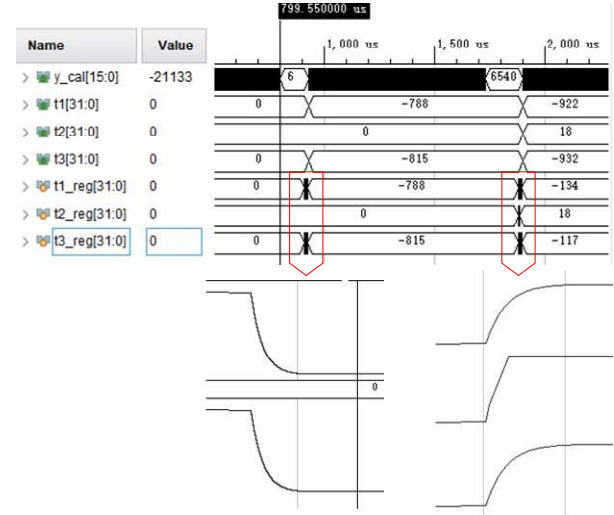


FIGURE 19. The simulation results of implementing the algorithm in Section III-B in Vivado.

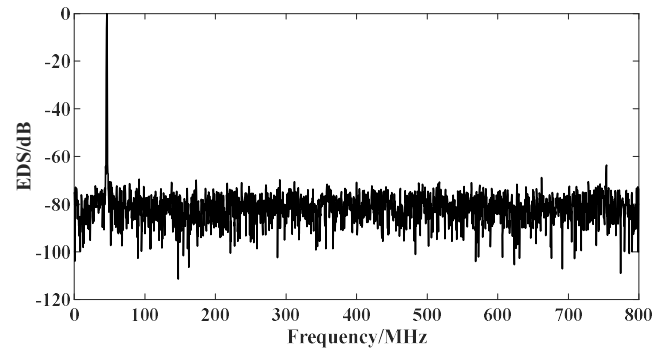


FIGURE 20. The frequency spectrum of the input signal after calibration in Vivado.

Since the simulation incorporates the input signal characteristics from the experiment, the number of samples L and the filter length are kept consistent with the simulation. Therefore, set the differential filter taps to 21. The number of samples used for each channel calibration is 2048. Finally, a smaller iteration step size was chosen to ensure the convergence of the LMS algorithm. Considering to use left and right shifting to implement multiplication operations for the iteration step size, the iterative step size is chosen to be 2^{-14} .

Fig. 19 shows the simulation results of the algorithm in Fig. 2, Fig. 3, and Fig. 5 implemented in Vivado. The results indicate that time skew values converge with each iteration. Fig. 20 depicts the frequency spectrum of the calibrated signal "y_cal" after FFT transformation. After calibrating the time skew in Vivado, the SNDR is 47.19dB, and the SFDR is 63.60dB. This demonstrates that the proposed algorithm can be effectively implemented in Vivado.

Fig. 21 shows the resources for estimating time skew by the proposed technique in Section III-B. It can be seen from Fig. 21 that there are 1509 look-up tables (LUTs), 1409 flip

TABLE VI
FPGA IMPLEMENTATION RESULTS

	[6]	[13]	[16]	[20]	[24]	[31]	This work
Device	XC7Z020 CLG484-1 SoC	XC7K325T FBG900-2	XC7vx485t ffg1157-1	EP4SGX230 KF40C2	XCVU37p- fsvh2892-2L-e	K7-KC705	XC7vx485t ffg1157-1
LUT	4166	4166	30480	8779	2197	8355	1509
RAM	66	-	13768	-	204	252	16.50
FF	7281	-	30576	-	1620	5476	1409
DSP	30	26	516	24	50	52	33

Utilization				
Post-Synthesis Post-Implementation				
Graph Table				
Resource	Utilization	Available	Utilization %	
LUT	1509	303600	0.50	
FF	1409	607200	0.23	
BRAM	16.50	1030	1.60	
DSP	33	2800	1.18	
IO	33	600	5.50	
BUFG	1	32	3.13	

FIGURE 21. The resources for estimating time skew by the proposed technique in Section III-B.

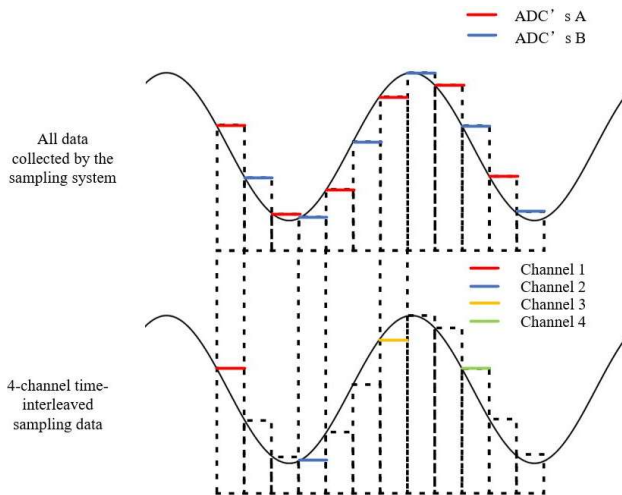


FIGURE 22. A 4-channel time-interleaved sampling data obtained by the sampling system in Fig. 13.

flops (FFs), 33 Inputs/Outputs (I/Os), 1 buffer-global-clock (BUFG), 33 digital signal processors (DSPs) and 16.5 block random access memories (BRAMs). The result demonstrates that this technique can be accomplished by few resources in the FPGA. Additionally, the estimated total on-chip power consumption of the estimation technique is 257mW, as reported by Vivado.

TABLE VI presents the resources required for implementing various advanced methods on FPGAs. The proposed method achieves the best performance in terms of LUT, RAM, and FF resources among the given options. The number of DSPs consumed is comparable to those in references [6], [13], and [20], and is less than those in references [20], [24] and [31]. Based on the results in the

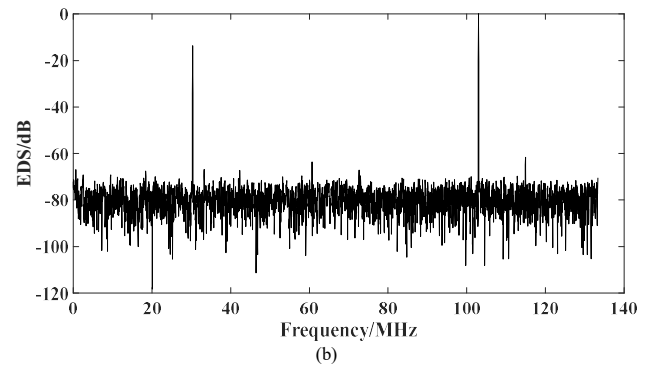
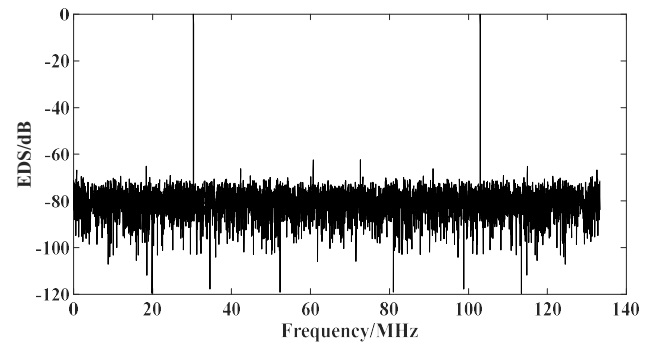


FIGURE 23. The frequency spectra before and after calibrating offset and gain: (a) the frequency spectrum before calibration; (b) the frequency spectrum after calibration.

table, it can be concluded that the proposed method performs well in terms of LUT, RAM, and FF resource consumption in hardware implementation. Furthermore, compared to the state-of-the-art technique using first-order statistics [31], the proposed calibration method successfully reduces DSP consumption by 19(36.54%) by decreasing computational complexity during iteration.

C. THE CALIBRATION OF EXPERIMENTAL DATA

The pre-calibration data of the dual-channel time-interleaved system can be obtained from Section V-A. However, the simulation was conducted in a 4-channel system, which may be confusing. For clarity, the collected dual-channel data can be split into a 4-channel system. Specifically, channels 1 and 3 are derived from the odd and even columns of the data collected by ADC's A, respectively. Similarly, channels 2 and 4 are derived from the odd and even columns of the data collected by ADC's

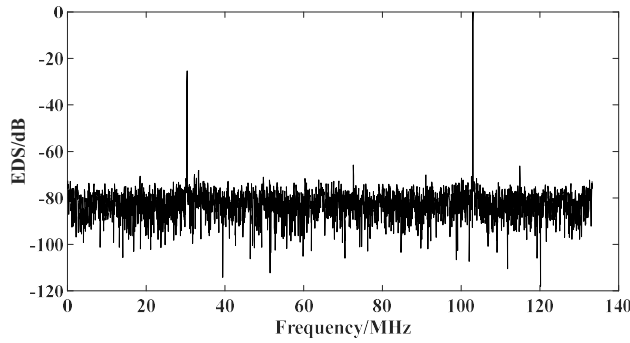


FIGURE 24. The frequency spectrum after rough calibration of time skew.

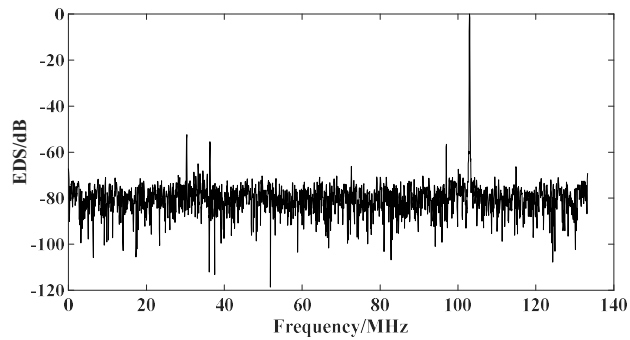


FIGURE 25. The frequency spectrum after calibrating time using the algorithm proposed in Section III-B.

B, respectively.

As the signal generator can only produce sinusoidal signals below 300MHz, while the sampling frequency of the system is 800MHz. To make the input signal during the simulation process closer to the frequency ($0.388f_s$), we can consider reducing the system's sampling frequency f_s . Fig. 22 demonstrates the results of a 4-channel data acquisition achieved through down sampling of collected data points. By this means, the sampling frequency is reduced from 800MHz to 800/3MHz.

A sinusoidal signal is generated by SDG6032X. The peak-to-peak voltage is 0.30V, the frequency is 103MHz($0.39f_s$). Then, this signal is converted from an analog signal to a digital signal in the ADC12DL3200EVM. The actual sampling rate of TI-ADCs is set to 800Mps.

After calibrating the offset and gain using the method in Section IV-A, the frequency spectra before and after calibration are shown in Fig. 23. After calibrating the offset and gain, the SNDR is 13.76dB and the SFDR is 25.36dB. The SNDR and SFDR values indicate that the time skew in the system may be large. Using Taylor series approximation method may introduce substantial approximation errors, which may invalidate the proposed calibration algorithm. Therefore, after calibrating the offset and gain, the method in [9] is adopted to rough calibrate time skew. The frequency spectrum after calibration is shown in Fig. 24.

In Fig. 24, the SNDR is 25.36dB and the SFDR is

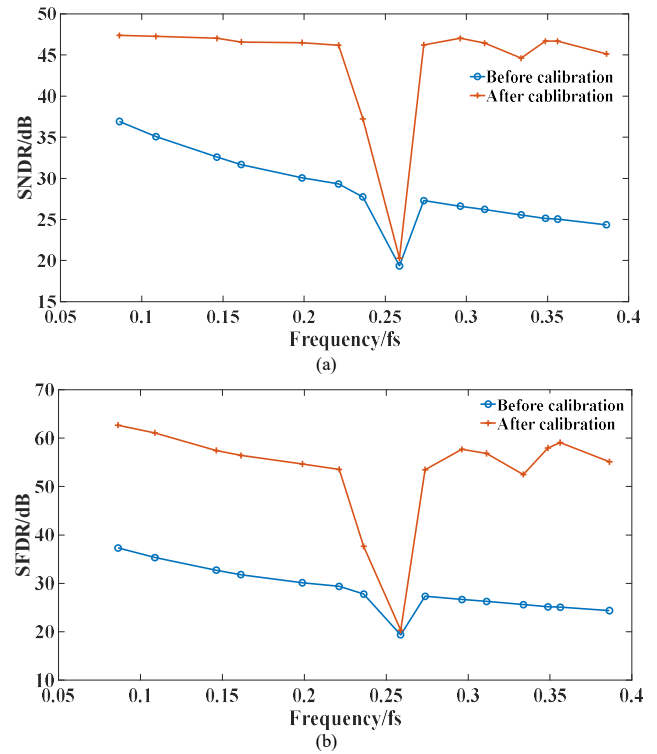


FIGURE 26. The performance of the frequency modulation signal: (a) the SNDR before and after calibration; (b) the SFDR before and after calibration.

25.39dB. As can be seen from Fig. 24, there is still a certain amount of time skew after calibration. The roughly calibrated data is then subject to precise calibration using the method proposed in Section III-B. The calibrated frequency spectrum is shown in Fig. 25. It can be observed from Fig. 25 that the spurious signals caused by time skew have been reduced after calibration. The SNDR after calibration is 45.33dB, and the SFDR is 55.34dB.

Fig. 26 shows the SNDR and SFDR of sinusoidal signals with different frequencies before and after calibration using the proposed method. From Fig. 26, it can be observed that the proposed calibration algorithm becomes ineffective when the input signal frequency is around $0.25f_s$. This is primarily due to the failure of the fractional delay filter employed in the algorithm presented in [9]. This leads to the overall algorithm's ineffectiveness at frequencies around $0.25f_s$. Disregarding the frequency points where the algorithm fails, as the input signal frequency increases, the SNDR before calibration decreases from approximately 36dB to around 25dB, while the SNDR after calibration remains above 44dB. Additionally, when the input signal frequency is 103MHz ($0.39f_s$), the calibrated SNDR is 45.33dB, and the SFDR is 55.34dB. This demonstrates that the proposed algorithm can effectively reduce time skew, thereby enhancing the performance of the time-interleaved sampling system.

The above simulations and experiments demonstrate that the proposed calibration algorithm has an effective

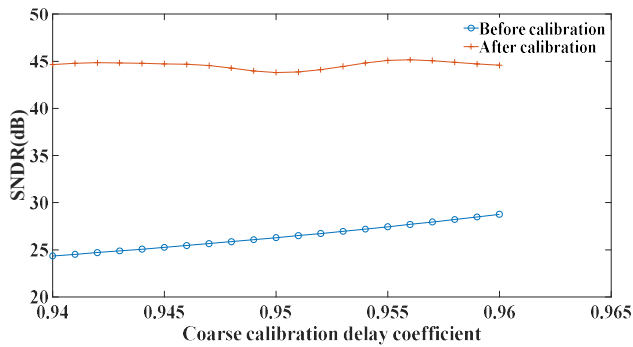


FIGURE 27. The frequency spectrum after calibrating time using the algorithm proposed in Section III-B.

calibration effect on a system with exact mismatches. However, it is still unknown how the algorithm performs in the face of different time-interleaved sampling systems with varying degrees of time skew. To demonstrate the robustness of the algorithm to time skew, the coarse calibration delay value can be varied to realize time-interleaved sampling systems with different time skew. Fig. 27 shows the Signal-to-Noise and Distortion Ratio (SNDR) before and after calibrating time skew using the proposed calibration algorithm, when the input signal is 103 MHz and the coarse calibration delay value ranges from 0.94 to 0.96. The results indicate that the SNDR of the system after calibration stabilizes at around 45 dB when the system contains different time skew. This demonstrates the robustness of the algorithm to time skew and reflects the robustness of the selected parameters to time-interleaved sampling systems with different mismatches.

VI. CONCLUSION

In this paper, we have successfully developed a low-complexity algorithm tailored to time skew calibration. By approximating absolute values, we decoupled the derivatives from the step size factor, achieving significant computational savings during convergence. Furthermore, an enhanced multi-stage feedback technique mitigated Taylor series approximation errors without compromising derivative calculation efficiency. Our algorithm demonstrated superior signal quality, evident in the enhanced SNDR and SFDR for various signals. Experimental validation confirmed its efficacy, while efficient resource utilization underscored its practicality for hardware implementation. In summary, it offers a promising solution to time skew calibration. However, due to limited knowledge of system-on-a-chip (SOC) designs, the algorithm has not been implemented and optimized on an SOC. Future work will focus on integrating the proposed algorithm onto an SOC, aiming at optimal power consumption and chip area design. Furthermore, the proposed algorithm requires the input signal to satisfy certain mathematical characteristics. How to combine the foreground calibration technique with the proposed

algorithm to obtain a method that relaxes the mathematical characteristics of the input signal is also a very meaningful topic.

REFERENCES

- [1] W. Black and D. Hodges, "Time interleaved converter arrays," *1980 IEEE International Solid-State Circuits Conference. Digest of Technical Papers*, San Francisco, CA, USA, 1980, pp. 14-15.
- [2] S. Singh, M. Epp, G. Valiant, M. Valkama and L. Anttila, "2-channel Time-Interleaved ADC frequency response mismatch correction using adaptive I/Q signal processing," *2013 IEEE 56th International Midwest Symposium on Circuits and Systems (MWSCAS)*, Columbus, OH, USA, 2013, pp. 1079-1084.
- [3] O. Järvinen, I. Kempf, V. Unnikrishnan, K. Stadius, M. Kosunen and J. Rynänen, "Fully Digital On-Chip Wideband Background Calibration for Channel Mismatches in Time-Interleaved Time-Based ADCs," *IEEE Solid-State Circuits Letters*, vol. 5, pp. 9-12, 2022.
- [4] Y. A. Tavares, S. Kim and M. Lee, "A Greedy Search Approach for Time-Interleaved ADCs Calibration Based on NRZ Input Patterns," *IEEE Transactions on Circuits and Systems I: Regular Papers*, vol. 69, pp. 1240-1251, 2022.
- [5] M. Guo, J. Mao, S. -W. Sin, H. Wei and R. P. Martins, "A 1.6-GS/s 12.2-mW Seven-/Eight-Way Split Time-Interleaved SAR ADC Achieving 54.2-dB SNDR With Digital Background Timing Mismatch Calibration," *IEEE Journal of Solid-State Circuits*, vol. 55, pp. 693-705, 2020, doi: 10.1109/JSSC.2019.2945298.
- [6] V.-T. Ta and V.-P. Hoang, "An Improved All-Digital Background Calibration Technique for Channel Mismatches in High-Speed Time-Interleaved Analog-to-Digital Converters," *Electronics* 2020, 9, 73.
- [7] M. Wahab and B. C. Levy, "Quadrature Filter Approximation for Reconstructing the Complex Envelope of a Bandpass Signal Sampled Directly With a Two-Channel TIADC," *IEEE Transactions on Circuits and Systems II: Express Briefs*, vol. 69, pp. 3017-3021, 2022.
- [8] Z. Lu, W. Zhang, H. Tang and X. Peng, "A Novel Two-Stage Timing Mismatch Calibration Technique for Time-Interleaved ADCs," *IEEE Transactions on Very Large Scale Integration (VLSI) Systems*, vol. 31, pp. 887-891, 2023.
- [9] Hu, M.; Yi, P., "Digital Calibration for Gain, Time Skew, and Bandwidth Mismatch in Under-Sampling Time-Interleaved System," *Appl. Sci.* 2022, 12, 11029, doi:10.3390/app122111029.
- [10] Xie, X.; Chen, H.; Yin, Y.; Wang, J.; Li, L.; Deng, H.; Meng, X., "All-digital calibration algorithm based on channel multiplexing for TI-ADCs," *Microelectron. J.* 2022, 126, 105503, doi: 10.1016/j.mejo.2022.105503.
- [11] H. Le Duc, D. M. Nguyen, C. Jabbour, P. Desgreys, O. Jamin and V. Tam Nguyen, "Fully Digital Feedforward Background Calibration of Clock Skews for Sub-Sampling TIADCs Using the Polyphase Decomposition," *IEEE Transactions on Circuits and Systems I: Regular Papers*, vol. 64, no. 6, pp. 1515-1528, June 2017, doi: 10.1109/TCSI.2016.2645978.
- [12] M. Wahab and B. C. Levy, "Direct Complex Envelope Sampling of Bandpass Signals With M-Channel Time-Interleaved ADCs," *IEEE Transactions on Signal Processing*, vol. 70, pp. 4804-4819, 2022.
- [13] Y. Qiu, Y. -J. Liu, J. Zhou, G. Zhang, D. Chen and N. Du, "All-Digital Blind Background Calibration Technique for Any Channel Time-Interleaved ADC," *IEEE Transactions on Circuits and Systems I: Regular Papers*, vol. 65, pp. 2503-2514, 2018.
- [14] J. Fan, Q. Li and G. Li, "Blind adaptive calibration of timing error for two-channel time-interleaved ADCs," *2010 53rd IEEE International Midwest Symposium on Circuits and Systems*, Seattle, WA, USA, 2010, pp. 233-236.
- [15] K. M. Tsui and S. C. Chan, "New Iterative Framework for Frequency Response Mismatch Correction in Time-Interleaved ADCs: Design and Performance Analysis," *IEEE Transactions on Instrumentation and Measurement*, vol. 60, pp. 3792-3805, 2011.
- [16] Y. Li et al, "Error Detection and Correction of Mismatch Errors in M-Channel TIADCs Based on Genetic Algorithm Optimization," *Electronics*, vol. 11, pp. 2366, 2022.
- [17] A. Khakpour and G. Karimian, "A New Fast Convergent Blind Timing Skew Error Correction Structure for TIADC," *IEEE Transactions on*

- Circuits and Systems II: Express Briefs*, vol. 68, pp. 1512-1516, 2021, doi: 10.1109/TCSII.2020.3023810.
- [18] Ali Khakpour and Ghader Karimian, "An Oversampling-Based Fast Convergent Blind Technique for Gain Mismatch and Timing Skew Error Correction in Time-Interleaved ADCs" *Circuits, Systems, and Signal Processing*, vol. 42, pp. 2416-2432, 2022.
- [19] H. L. Duc, C. Jabbour, P. Desgreys, O. Jamin and N. Van Tam, "A fully digital background calibration of timing skew in undersampling TI-ADC," *2014 IEEE 12th International New Circuits and Systems Conference (NEWCAS)*, Trois-Rivieres, QC, Canada, 2014.
- [20] H. Le Duc et al., "All-Digital Calibration of Timing Skews for TIADCs Using the Polyphase Decomposition," *IEEE Transactions on Circuits and Systems II: Express Briefs*, vol. 63, pp. 99-103, 2016.
- [21] J. Li, S. Wu, Y. Liu, N. Ning and Q. Yu, "A Digital Timing Mismatch Calibration Technique in Time-Interleaved ADCs," *IEEE Transactions on Circuits and Systems II: Express Briefs*, vol. 61, pp. 486-490, 2014.
- [22] M. Yin and Z. Ye, "First Order Statistic Based Fast Blind Calibration of Time Skews for Time-Interleaved ADCs," *IEEE Transactions on Circuits and Systems II: Express Briefs*, vol. 67, pp. 162-166, 2020.
- [23] Zhao, C., Diao, J., Xu, H. et al. "Correlation-based reconfigurable blind calibration for timing mismatches in TI-ADCs," *Analog Integr Circ Sig Process*, vol. 107, pp. 29-38, 2021.
- [24] S. Liu, L. Zhao and S. Li, "A Novel All-Digital Calibration Method for Timing Mismatch in Time-Interleaved ADC Based on Modulation Matrix," *IEEE Transactions on Circuits and Systems I: Regular Papers*, vol. 69, pp. 2955-2967, 2022.
- [25] D. Li, L. Zhao, L. Wang, Y. Shen and Z. Zhu, "A Fast Convergence Second-Order Compensation for Timing Skew in Time-Interleaved ADCs," *IEEE Transactions on Very Large Scale Integration (VLSI) Systems*, vol. 30, pp. 1558-1562, 2022.
- [26] M. Guo, S. -W. Sin, L. Qi, D. Xu, G. Wang and R. P. Martins, "Background Timing Mismatch Calibration Techniques in High-Speed Time-Interleaved ADCs: A Tutorial Review," in *IEEE Transactions on Circuits and Systems II: Express Briefs*, vol. 69, no. 6, pp. 2564-2569, June 2022.
- [27] X. Li, J. Wu and C. Vogel, "A background correlation-based timing skew estimation method for time-interleaved ADCs," in *IEEE Access*, vol. 9, pp. 45730-45739, 2021.
- [28] V.-P. Hoang and V.-T. Ta, "Fully digital background calibration of channel mismatches in time-interleaved ADCs using recursive least square algorithm," *AEU-International J. of Electronics and Communications*, vol. 130, 2021.
- [29] Y. Wang, H. Johansson, M. Deng and Z. Li, "On the compensation of timing mismatch in two channel time-interleaved ADCs: Strategies and a novel parallel compensation structure," *IEEE Trans. Signal Processing*, vol. 70, pp. 2460-2475, 2022.
- [30] M. Guo, J. Mao, S. -W. Sin, H. Wei and R. P. Martins, "A 5 GS/s 29 mW Interleaved SAR ADC With 48.5 dB SNDR Using Digital-Mixing Background Timing-Skew Calibration for Direct Sampling Applications," in *IEEE Access*, vol. 8, pp. 138944-138954, 2020.
- [31] Xu W, Yao B, Cheng Q, et al, "A Reference Assisted Background Calibration Technique With Constant Input Impedance for Time-Interleaved ADCs," in *IEEE Transactions on Circuits and Systems II: Express Briefs*, 2024.



Min Hu was born in Xiaogan, China, in 1999. He received the B.S. degree in Mechatronic Engineering from Wuhan University of technology, Wuhan, China, in 2019. He is currently working toward the Ph.D. degree in mechanical engineering in Huazhong University of Science & Technology, Wuhan, China. His research interest is digital signal processing.

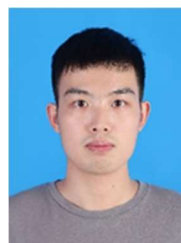


Zhengxu Hao was born in Changchun, China, in 1998. He graduated from the School of Mechanical and Aerospace Engineering, Jilin University in 2021. Now he is studying for a master's degree in the School of Mechanical Science and Engineering, Huazhong University of Science and Technology, focusing on signal processing.



Pengxing Yi (Senior Member, IEEE) was born in Changde, China, in 1974. He received the B.S. degree in Mechatronic Engineering from Wuhan University of Science & Technology, Wuhan, China, in 1997, and the M.S. and Ph.D. degrees in Mechanical Engineering from Huazhong University of Science & Technology, Wuhan, China in 2003 and 2007. From 2007 to 2009, he is a post Doctoral research fellow in the Department of Control Science and Engineering,

Huazhong University of science & Technology, Wuhan, China. Since 2009, he has been an associate professor in the School of Mechanical Science & Engineering, Huazhong University of Science & Technology, Wuhan, China. From 2013 to 2014, he was a visiting professor at Georgia Institute of Technology, Atlanta, GA, USA. His research Interests include NDT, high speed data acquisition and signal processing, intelligent monitoring methods in manufacturing.



Zhitong Zhou was born in Chongzuo, China, in 2000. He received the B.S. degree in Mechatronic Engineering from Huazhong University of Science & Technology, Wuhan, China, in 2022. He is currently studying for a M.S. degree in Huazhong University of Science & Technology. His research Interest is high speed data acquisition and signal processing.